

# Excitonic and biexcitonic properties of single GaN quantum dots modeled by 8-band $k \cdot p$ theory and configuration-interaction method

Stanko Tomić\*

*Computational Science and Engineering Department, STFC Daresbury Laboratory, Cheshire WA4 4AD, United Kingdom*

Nenad Vukmirović

*Computational Research Division, Lawrence Berkeley National Laboratory, Berkeley, California 94720, USA*

(Received 2 March 2009; published 26 June 2009)

Excitons and biexcitons in GaN/AlN quantum dots (QD) were investigated with special emphasis on the use of these QDs for single-photon source applications. The theoretical methodology for the calculation of single-particle states was based on 8-band strain-dependent envelope function Hamiltonian, with the effects of spin-orbit interaction, crystal-field splitting, and piezoelectric and spontaneous polarizations taken into account. Exciton and biexciton states were found using the configuration-interaction method. Optimal QD heights for their use in single-photon emitters were determined for various diameter to height ratios. The competition between strong confinement in GaN QDs and internal electric field, generally reported in wurtzite GaN, was also discussed, as well as its effect on appearance of bound biexcitons.

DOI: 10.1103/PhysRevB.79.245330

PACS number(s): 73.21.La, 78.67.Hc

## I. INTRODUCTION

For further improvements in the operation of optoelectronic devices based on GaN/AlN quantum dots (QD), it is important to better understand the excitonic structure of the dots, and, in particular, its inter-relationship with QD geometry. This is a challenging task since in addition to the effects of quantum confinement, strain, band mixing, and electron-hole Coulomb interaction present in any quantum-dot system, wurtzite GaN/AlN quantum dots exhibit strong built-in electric fields induced due to spontaneous and piezoelectric polarizations.<sup>1,2</sup>

Modern optoelectronic devices like triggered single-photon sources (“photon on demand”) are highly desired for applications in quantum-cryptography and quantum-information processing.<sup>3</sup> One of the routes for realization of compact single-photon devices is to use an excitonic transition in a single QD. Such devices were initially realized based on InAs/GaAs quantum-dot material system.<sup>4,5</sup> Sources of triggered entangled photons emitted from the biexcitonic cascade decay were also realized.<sup>6,7</sup> Moreover, theoretical proposals suggest that an exciton state in a GaN quantum dot could be used as a qubit in quantum computer architectures.<sup>8</sup>

GaN/AlN quantum dots<sup>9–11</sup> offer certain advantages for realization of single-photon sources. Larger band offsets and effective masses lead to strong quantum-confinement effects which should enable the operation of single-photon sources at higher temperatures. Several single III-nitride quantum-dot spectroscopy experiments were therefore performed,<sup>12–15</sup> which indeed led to the realization of a GaN/AlN single-photon source operating at 200 K.<sup>16</sup> Recent studies also consider polarization properties of single GaN/AlN QDs.<sup>17,18</sup> It is interesting to note the variety of other possible applications of GaN quantum dots: wide band gap of III-nitrides leads to the emission in the blue and ultraviolet spectral range,<sup>19,20</sup> which is not accessible with most of the other materials and also provides for room-temperature emitters at telecommunication wavelengths.<sup>21</sup>

For single-photon source applications it is desirable to have as large as possible the value of biexcitonic shift defined as the difference between the energy of the transition line from the biexciton to exciton state and the energy of the exciton transition line. This is required to enable good spectral separation of the two lines.<sup>16</sup> It is known<sup>11,22</sup> that the built-in electric field acts to localize the electrons at the top of the dot and holes at the bottom of the dot. Consequently, the interaction between two excitons forming a biexciton is mostly determined by repulsive electron-electron and hole-hole interactions which are stronger than the attractive interaction between spatially separated electron and hole.<sup>15,23</sup> For quantum dots with larger heights the biexciton is therefore certainly unbound and biexcitonic shift increases as the height increases due to a decreasing attractive part of the interaction. From that perspective, it is desirable to have a large QD height. On the other hand, one should also have the optical transition matrix element of the exciton transition as large as possible.<sup>13</sup> For large quantum dots, this element is small due to spatial separation of electron and hole wave functions,<sup>22</sup> and it is therefore desirable to have a small quantum-dot height from this perspective. This discussion therefore indicates that the appropriate quantum-dot geometry for single-photon-source applications should be determined as a compromise between the two opposite requirements, which requires detailed knowledge of the excitonic properties of these dots.

The biexcitonic shift is a sensitive probe of QD geometry, the nature of electron-hole, and exchange interaction.<sup>24</sup> In a recent single GaN/AlN dot spectroscopy experiment,<sup>15</sup> the existence of bound biexcitons (that appear when the energy of the biexciton ground state is lower than twice the energy of the exciton ground state) for small dots was observed. Similar effect was found in the case of disk shaped GaN/AlN quantum dots in GaN nanowires.<sup>25</sup> The appearance of bound biexcitons can not be described in the framework of the Hartree approximation which does not include the effect of electron-exchange-correlation interaction.<sup>15,26</sup> Theoretical

studies of excitons and biexcitons in nitride quantum dots were usually based on Hartree approximation,<sup>18,23,27</sup> while several works<sup>28–30</sup> that use the full configuration-interaction method (in combination with tight-binding calculation of single-particle states) did not address the issue of the sign of the biexcitonic shift and treat different material system, i.e., InN/GaN.

Motivated to understand the physics of single-photon source devices<sup>16</sup> and the spectroscopic signatures of single GaN/AlN dots,<sup>15</sup> we present theoretical calculations of the exciton and biexciton states. We identified the reasons why optimal GaN single-photon source devices emit around 3.5 eV. We found that the appearance of bound biexcitons in small GaN/AlN quantum dots can only be explained if the coefficients of the spontaneous and piezoelectric polarization, widely accepted for the bulk or wide quantum-well structures<sup>1</sup> are strongly reduced in such small dots. Indeed, recent experimental findings suggest that the small size of the QDs seems to prevent the carriers from being affected by the strong built-in electric fields generally reported for III-nitrides wurtzite materials, which could be an alternative solution to nonpolar nitride QDs.<sup>31</sup>

The paper is organized as follows: in Sec. II, we review a theoretical model developed for the calculation of the electronic and excitonic structure of the single GaN/AlN QDs in wurtzite (hexagonal) crystal structure. In Sec. III we present our results and discuss: the optimal size of hexagonal supercell used in the calculation of the Coulomb integrals in GaN QDs, Sec. III A; the influence of spin-orbit interaction on the excitonic structure of the GaN QDs, Sec. III B; the optimization procedure for design of the single-photon sources based on GaN QDs, Sec. III C; and the influence of the internal built-in electric fields on the exciton binding in small GaN QDs, Sec. III D. In Sec. IV we draw conclusions.

## II. THEORETICAL CONSIDERATIONS

To gain insight into the excitonic properties of single GaN quantum dots, we have performed calculations using the methodology that is described below. Quantum dots in the shape of hexagonal truncated pyramid were considered.<sup>16</sup> It is assumed that the QD is positioned on the wetting layer (WL) and embedded in three nested hexagonal prisms, (Fig. 1) which were introduced for the single QD calculation purpose, as will be described. The dimensions of the QD are controlled by two independent parameters: the diameter  $D$  of the circumscribed circle around the hexagon at the WL-QD interface at  $z=0$ , and the angle  $\alpha$  between pyramid base and pyramid side edges. The size of the QDs was controlled by  $D/h$  aspect ratio, where  $h$  is the QD height. Dimensions of the two nested embedding boxes in the form of hexagonal prisms are defined by the base diameter  $D_v$ , the height  $H_v$ , and the volume  $\Omega_v$ . The subscript  $v=e$  is related to a smaller supercell used in the expansion of the kinetic part of the Hamiltonian; and subscript  $v=s$  is related to large supercell on which the strain, spontaneous, and piezoelectric polarizations were calculated. The third embedding box used in calculation of the Coulomb integrals, ( $v=c$ ), is made to be of a more isotropic shape to better capture the isotropy of the

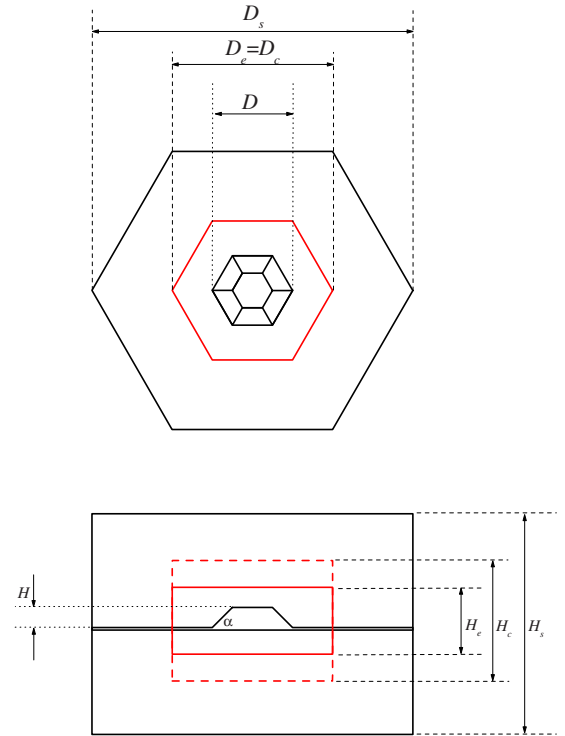


FIG. 1. (Color online) Schematic diagram of GaN/AlN QD in the shape of a truncated hexagonal pyramid, embedded in three “Russian doll” type nested embedding boxes that are used for electronic structure, strain, and Coulomb integral calculations as described in the main text.

Coulomb interaction. We discuss its shape and size in more detail in Sec. III A.

Single-particle electron and hole states of GaN QDs were modeled using the 8-band  $\mathbf{k}\cdot\mathbf{p}$  Hamiltonian,<sup>32</sup> consisting of the kinetic part that includes spin-orbit interaction, the crystal-field splitting, the strain part, and additional terms arising from the presence of spontaneous and piezoelectric polarization. Material parameters in the Hamiltonian were taken from Ref. 33.

In many works,<sup>11,34</sup> the 8-band  $\mathbf{k}\cdot\mathbf{p}$  Hamiltonian is simplified by neglecting the spin-orbit interaction. Although it has relatively small values in III-nitrides ( $\sim 10\text{--}20$  meV) when compared to the fundamental energy gap at the  $\Gamma$  point ( $>2$  eV), the spin-orbit interaction splits the fourfold-degenerate top valence band ( $\Gamma_6$  symmetry) into two twofold-degenerate bands ( $\Gamma_9$  and  $\Gamma_7$ ).<sup>35,36</sup> Consequently this simplification leads to block diagonalization of the Hamiltonian into two identical 4-band Hamiltonians. For the present work we choose the more sophisticated 8-band Hamiltonian. The main reason is that in hexagonal quantum dots the 4-band Hamiltonian leads to a doubly degenerate ground hole state<sup>34</sup> which is split by the spin-orbit interaction in 8-band Hamiltonian.<sup>37</sup> Since the main focus of the paper will be on ground exciton and biexciton states, we find it very important to correctly predict the degeneracies of ground electron and hole state since these states largely determine the ground (bi)exciton properties.

The eigenvalue problem of the single-particle Hamiltonian was solved using the plane-wave (PW) method.<sup>11</sup>

While there are quite a few advantages in using the plane-wave method,<sup>11,38</sup> we emphasize that there are several issues that need to be resolved if one wants to apply the method to single GaN/AlN quantum-dot calculations. Within the straightforward PW approach, due to the presence of large built-in electric fields that decay slowly away from the dot, a very large supercell would be required to correctly describe the potential due to these fields. This is undesirable since a very large plane-wave basis set would then be required to describe the wave functions which are well localized to the dot region.

A better approximation for strain distribution of a single dot is obtained if a box  $\Omega_s$  larger than  $\Omega_e$  is used for calculating the Fourier transform of the strain distribution  $\epsilon_{ij}^{(s)}(\mathbf{K})$ , for which analytic expressions<sup>11</sup> exist. These quantities are then renormalized to a small supercell,  $\Omega_e$ , by interpolation in inverse space,

$$\epsilon_{ij}^{(e)}(\mathbf{k}) = \frac{1}{\Omega_s} \sum_{\mathbf{K} \in \text{inv}\Omega_s} \epsilon_{ij}^{(s)}(\mathbf{K}) \int_{\Omega_e} e^{i(\mathbf{K}-\mathbf{k})\cdot\mathbf{r}} d^3\mathbf{r}. \quad (1)$$

It means also that one will use two sets of PWs: the *augmented* set  $(n_x^{(s)}, n_y^{(s)}, n_z^{(s)})$  related to the box  $\Omega_s$  and denoted as  $\mathbf{K}$  and conventional set  $(n_x^{(e)}, n_y^{(e)}, n_z^{(e)})$  related to the box  $\Omega_e$  and denoted as  $\mathbf{k}$ . The piezoelectric field is described with

$$V_{\text{PZ}}^{(e)}(\mathbf{k}) = -i \frac{1}{\epsilon k^2} \{ 2[k_x \epsilon_{xz}^{(e)}(\mathbf{k}) + k_y \epsilon_{yz}^{(e)}(\mathbf{k})] d_{15} + k_x [\epsilon_{xx}^{(e)}(\mathbf{k}) + \epsilon_{yy}^{(e)}(\mathbf{k})] d_{13} + k_z \epsilon_{zz}^{(e)}(\mathbf{k}) d_{33} \} + \delta V_{\text{PZ}}^{(e)}(\mathbf{k}), \quad (2)$$

where term  $\delta V_{\text{PZ}}^{(e)}(\mathbf{k})$  is obtained by replacing QD piezoelectric coefficients  $d_{ij}$  with the difference between QD and barrier value of the piezoelectric coefficients,  $d_{ij} \rightarrow \Delta d_{ij}$ , and strain elements with its convolution with characteristic QD shape function,  $\epsilon_{ij}^{(e)}(\mathbf{k}) \rightarrow \sum_{\mathbf{k}'} \chi(\mathbf{k}-\mathbf{k}') \epsilon_{ij}^{(e)}(\mathbf{k}')$ . Since piezoelectric field, Eq. (2), is the function of the strain tensor elements,  $\epsilon_{ij}^{(e)}(\mathbf{k})$  given by Eq. (1), only, its effect automatically follows the one of the strain. The long-range potential due to spontaneous polarization is also calculated by using interpolation in the inverse space,

$$V_{\text{SP}}^{(e)}(\mathbf{k}) = -i \Delta(P_{\text{SP}}/\epsilon) \chi(\mathbf{k}) \left( \frac{1}{\Omega_s} \sum_{\mathbf{K} \in \text{inv}\Omega_s} \frac{K_z}{K^2} \int_{\Omega_e} e^{i(\mathbf{K}-\mathbf{k})\cdot\mathbf{r}} d^3\mathbf{r} \right), \quad (3)$$

where  $\Delta(P_{\text{SP}}/\epsilon)$  is the difference between values of QD and barrier material spontaneous polarization coefficient divided by permittivity and  $\chi(\mathbf{k})$  is the characteristic QD shape function in the  $\mathbf{k}$  space. Expressions (1)–(3) gives better approximation for  $\epsilon_{ij}(\mathbf{k})$ ,  $V_{\text{PZ}}(\mathbf{k})$ , and  $V_{\text{SP}}(\mathbf{k})$ , of a single QD structure, and can be systematically improved by making  $\Omega_s$  sufficiently large to eliminate the strain, piezoelectric, and spontaneous polarization fields propagation from neighboring dots that are artificially introduced due to periodic boundary conditions. As such they are used in the construction of the PW representation of the single QD Hamiltonian. This leads to a much smaller plane-wave basis set,  $\mathbf{k}$ , than the one that would be required if the kinetic part of the

Hamiltonian were expanded using  $\mathbf{K}$ . More elaborate discussion of the method can be found in Ref. 38.

In the previous works,<sup>11,18,39</sup> a cubic embedding box was used for wurtzite QD structures. The symmetry of the model is defined by the highest symmetry subgroup that is common to the symmetries of the QD shape, the embedding box, and the symmetry of the model  $\mathbf{k} \cdot \mathbf{p}$  Hamiltonian. When the symmetry of the QD shape is  $C_{6v}$  for hexagonally shaped QDs, and the symmetry of the cubic embedding box is  $O_h$ , the common subgroup is  $C_{2v}$ . Consequently, the numerical solutions do not capture the right symmetry of the  $\mathbf{k} \cdot \mathbf{p}$  Hamiltonian for wurtzite QD structures (which is  $C_{6v}$  instead of  $C_{2v}$ ). Such a set of single-particle states can lead to additional artifacts once imported in excitonic-structure calculations. Therefore, a hexagonally shaped embedding box is used in our calculations and plane waves adapted to such box are implemented.<sup>34</sup> Our numerical solutions therefore capture the right  $C_{6v}$  symmetry of the model 8-band  $\mathbf{k} \cdot \mathbf{p}$  Hamiltonian even with limited basis sets. In the Appendix, we have shown how symmetry of the model can be exploited to significantly reduce computational costs without losing on accuracy.

We also note that the actual symmetry of a hexagonally shaped wurtzite GaN/AlN quantum dot is  $C_{3v}$  (Refs. 28 and 40) and can be captured either by modeling the strain using the atomistic valence force-field (VFF) model or by taking more bands in the  $\mathbf{k} \cdot \mathbf{p}$  Hamiltonian.<sup>41</sup> We will therefore discuss the consequences of using the model with a higher  $C_{6v}$  symmetry on the results, in Sec. III B.

After the single-particle states were found, the (bi)exciton states were obtained using the configuration-interaction method,<sup>38,42,43</sup> i.e., by direct diagonalization of the Hamiltonian<sup>44</sup>

$$\hat{H} = \sum \epsilon_i \hat{e}_i^\dagger \hat{e}_i - \sum \epsilon_i \hat{h}_i^\dagger \hat{h}_i + \frac{1}{2} \sum V_{iljk} \hat{e}_i^\dagger \hat{e}_j^\dagger \hat{e}_k \hat{e}_l + \frac{1}{2} \sum V_{iljk} \hat{h}_i^\dagger \hat{h}_j^\dagger \hat{h}_k \hat{h}_l - \sum (V_{iljk} - V_{ikjl}) \hat{e}_i^\dagger \hat{h}_j^\dagger \hat{h}_k \hat{e}_l, \quad (4)$$

where  $\hat{e}(\hat{e}^\dagger)$  are electron annihilation (creation) operators,  $\hat{h}(\hat{h}^\dagger)$  are the same operators for holes, and  $\epsilon_i$  are the single-particle energies. The summation over each index takes place over electron or hole states only depending whether that index corresponds to electron or hole operator. Coulomb integrals,  $V_{ijkl}$ , required for the diagonalization of the configuration-interaction (CI) Hamiltonian were evaluated in reciprocal space and then corrected using the Makov-Payne method<sup>38,45,46</sup> by adding the first few terms (monopole, dipole, and quadrupole) in the multipole expansion to compensate for the effect of the mirror charges induced by periodic boundary conditions. These read as

$$V_{ijkl} = V_{ijkl}(\Omega_c) - \frac{e^2}{4\pi\epsilon} \left[ q_{ij} q_{kl} a_{\text{mad}} + \frac{4\pi}{3\Omega_c} \mathbf{d}_{ij} \cdot \mathbf{d}_{kl} - \frac{2\pi}{3\Omega_c} (q_{ij} Q_{kl} + q_{kl} Q_{ij}) \right], \quad (5)$$

where  $V_{ijkl}(\Omega_c)$  is uncorrected Coulomb integral calculated on  $\Omega_c$ , and  $q_{ij}(\Omega_c) = \delta_{ij}$ ,  $d_{ij}(\Omega_c)$ , and  $Q_{ij}(\Omega_c)$  are the monopole, dipole, and quadrupole corrections, respectively, that acquire analytic form in the PW representation. The Madelung term in Eq. (5),  $a_{\text{mad}}$ , is defined via Ewald sums in real and inverse space, and self-interaction correction term as

$$a_{\text{mad}} = \sum_{\substack{\mathbf{R} \in \text{dir}\Omega_c \\ \mathbf{R} \neq 0}} \frac{\text{erfc}(R\eta^{1/2})}{R} + \frac{4\pi}{\Omega_c} \sum_{\substack{\mathbf{k} \in \text{inv}\Omega_c \\ \mathbf{k} \neq 0}} \frac{\exp(-k^2/4\eta)}{k^2} - 2\sqrt{\frac{\eta}{\pi}} - \frac{\pi}{\eta\Omega_c}. \quad (6)$$

The Ewald parameter  $\eta$  controls the rate of convergence of the sums. It was set in all calculations to  $\eta = \pi/[3\sqrt{3}(D_c/2)^2/2]$ . Depending on order of indices in Eq. (5) those integrals represent direct Coulomb integrals  $J_{ab} = V_{aabb}$  or exchange Coulomb integrals  $K_{ab} = V_{abab}$ . An efficient and accurate method to evaluate these expressions in reciprocal space was described in Ref. 38.

Additionally, symmetry considerations imply that only Coulomb integrals  $V_{ijkl}$  whose wave functions satisfy the conservation of the total quasiangular momentum,

$$\{m_j + m_l \equiv m_i + m_k \pmod{6}\} \quad (7)$$

are nonzero. These are therefore the only ones that need to be evaluated, which reduces the number of integrals that need to be calculated by a factor of 6.

The whole methodology presented here was implemented in the `kppw` code.<sup>47</sup>

### III. RESULTS AND DISCUSSION

To support our statements in next two subsections, Secs. III A and III B, we consider a model GaN/AlN QD with  $D = 10$  nm,  $h = 2$  nm, and  $\alpha = 30^\circ$  embedded in the boxes in the shape of hexagonal prisms with the dimensions  $D_e = 50$  nm and  $H_e = 10$  nm,  $D_s = 150$  nm, and  $H_s = 180$  nm. The lateral size of  $\Omega_c$  is  $D_c = 50$  nm while its vertical dimension is discussed in Sec. III A and adopted in the rest of the analysis.

#### A. Optimal supercell size for Coulomb integral calculation in a hexagonal QD

While the value of error between corrected and uncorrected expression for the direct Coulomb integrals,  $V_{ijkl} - V_{ijkl}(\Omega_c)$ , has  $\propto 1/L$  asymptotic behavior<sup>48</sup> in a cubic embedding box,<sup>38,45,46</sup> this is not necessarily the case when one treats hexagonally shaped embedding boxes. To identify the optimal size of the  $\Omega_c$  box, the influence of the embedding box elongation in the  $z$  direction on the convergence of the Coulomb integral  $J_{e0,h0}$  is shown in Fig. 2(a). It can be seen that the corrected value of  $J_{e0,h0}$ , calculated according to Eq. (5), monotonically approaches the actual value, calculated in real space, as  $H_c$  is increased. On the other hand, uncorrected value of  $J_{e0,h0}(\Omega_c)$  (the trend would be the same if one assumes  $\Omega_c \equiv \Omega_e$ , i.e., that  $\Omega_c$  coincides with box used for expansion of the kinetic part of the Hamiltonian as in conventional PW methods), exhibits a nonmonotonic behavior.

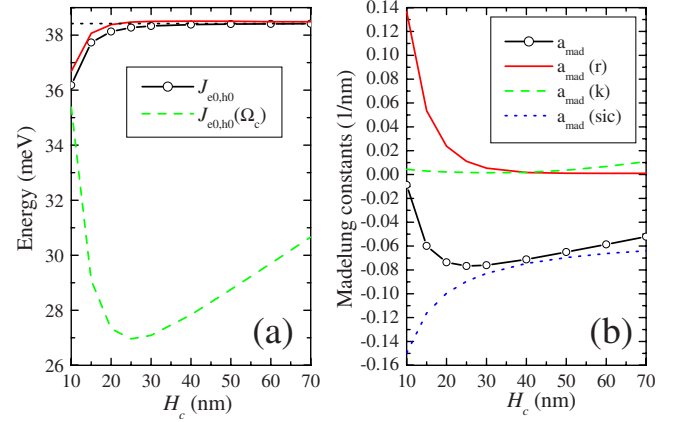


FIG. 2. (Color online) (a) The dependence of  $J_{e0,h0}$  integral on the  $H_c$  dimension of the  $\Omega_c$ : calculated without multipole corrections (dashed line), with monopole correction only (solid line), with all multipole corrections included (solid line with symbols), and actual value calculated in direct space (dotted line). (b) Dependence of the Madelung constant (solid line with symbols) and its components: the short range (solid line), long range (dashed line), and self-interaction (dotted line).

It decreases up to some critical point beyond which  $J_{e0,h0} - J_{e0,h0}(\Omega_c)$  again acquires the  $\propto 1/L$  trend. We have identified that the main correction to the direct Coulomb integrals calculated according to Eq. (5), is due to the monopole term which is proportional to  $\propto q_{ij}q_{kl}a_{\text{mad}}$ . It should be noted further, that for direct Coulomb integrals, such as  $J_{e0,h0}$ , the effective charges  $q_{e0,e0} = 1$  and  $q_{h0,h0} = 1$ . It means that the monopole correction is entirely determined by  $a_{\text{mad}}$  which depends on the  $\Omega_c$  box dimensions only and not on the overlap of the wave functions. The individual components of the Ewald sum, Eq. (6), are plotted in Fig. 2(b), as a function of  $H_c$ . It can be seen that the nonmonotonic shape of  $a_{\text{mad}}$  is actually determined by the interplay between short-ranged interaction component calculated in real space and self-energy interaction term. We conclude that the optimal value of the  $H_c$  at which direct Coulomb integrals approach actual values within  $< 0.4\%$  is 25 nm.

#### B. Symmetries of exciton states in GaN QDs and the effect of spin-orbit interaction

To explain the origin of the excitonic structure and to understand the possible differences of the results of our model and other models, we classify the single-particle states, exciton, and biexciton states according to symmetry. We follow the notation in Ref. 49. In the case when spin-orbit interaction is not included, the 8-band  $\mathbf{k} \cdot \mathbf{p}$  Hamiltonian splits into two identical 4-band Hamiltonians. The eigenstates of each of these are represented by single-valued irreducible representations (IRs) of the  $C_{6v}$  group. Our calculation shows that the highest state in the valence band ( $h0$ ) transforms according to two-dimensional IR  $E_1$  and the lowest state in the conduction band ( $e0$ ) transforms according to one-dimensional representation  $A_1$ . Therefore, including the twofold spin degeneracy,  $h0$  is fourfold degenerate and  $e0$  is twofold degenerate.

In the case when spin-orbit interaction is included, the eigenstates of the Hamiltonian transform according to double-valued IRs of the  $C_{6v}$  group. We find that  $h0$  transforms as  $\bar{E}_3$  and  $e0$  transforms as  $\bar{E}_1$ . Therefore both of them are twofold degenerate, indicating that spin-orbit interaction has split the fourfold degenerate  $h0$ . This demonstrates the importance of including spin-orbit interaction despite its relatively small value. The spin-orbit interaction is often neglected in  $\mathbf{k}\cdot\mathbf{p}$  (Refs. 11 and 34) and tight-binding calculations<sup>29,50</sup> which automatically then leads to the wrong dimensionality of ground exciton and biexciton manifolds.

We note that the  $C_{3v}$  symmetry (which is present if the strain is modeled using VFF within  $\mathbf{k}\cdot\mathbf{p}$ , the  $\mathbf{k}\cdot\mathbf{p}$  model that includes a larger number of bands,<sup>41</sup> or if tight-binding or empirical pseudopotential model is used) would yield the same degree of degeneracy of all the mentioned states, as one can easily check that the subduction procedure of each of the IRs of the  $C_{6v}$  group to the  $C_{3v}$  subgroup yields the IR of the same dimensionality.

We now proceed with the discussion of the excitonic structure. Exciton states transform according to single-valued IRs of the symmetry group.<sup>40</sup> The IRs corresponding to the states of the ground exciton manifold can be determined from the direct product of the IR of  $e0$  and complex conjugated IR of  $h0$ .<sup>40</sup> In the case when spin-orbit interaction is not included, this gives  $A_1 \otimes E_1 = E_1$ . Therefore, the orbital part of the exciton state transforms as  $E_1$ . The spins of an electron and a hole forming an exciton can form either the singlet or the triplet state. Therefore the ground eight-dimensional manifold consists of the doubly degenerate ground state (stemming from  $E_1$  symmetry of the orbital part and the singlet of the spin part) and sixfold degenerate excited state (stemming from  $E_1$  symmetry of the orbital part and the triplet of the spin part). An  $E_1$  exciton is allowed to emit  $xy$ -polarized radiation while it is not allowed to emit  $z$ -polarized radiation. On the other hand, due to conservation of spin in the optical transition, the singlet state is dark, while in the triplet two states are bright and one is dark. This implies that the twofold-degenerate ground exciton state is dark while the sixfold degenerate excited state consists of four bright and two dark states. We note again that the considerations of the full  $C_{3v}$  would yield exactly the same conclusions related to the degeneracy of states and allowed optical transitions.

In the case when spin-orbit interaction is included, the symmetry of states in the four-dimensional exciton manifold is determined from  $\bar{E}_1 \otimes \bar{E}_3 = E_1 + E_2$ . Therefore it consists of the twofold-degenerate  $E_2$  exciton and the twofold-degenerate  $E_1$  exciton.  $E_2$  exciton is dark while  $E_1$  exciton can emit  $xy$ -polarized radiation. Our calculation yields that  $E_2$  exciton has a lower energy than  $E_1$ . The subduction of  $E_2$  representation to the  $C_{3v}$  subgroup yields the  $E$  representation which allows for emission of  $xy$ -polarized radiation. Consequently, the ground exciton state that we find to be dark may become weakly bright if the full  $C_{3v}$  symmetry is considered.

Next, we discuss the allowed optical transitions for all exciton states. The  $C_{6v}$  group has six single-valued IRs  $A_1$ ,  $B_2$ ,  $A_2$ ,  $B_1$ ,  $E_1$ , and  $E_2$ . The  $A_1$  excitons are allowed to emit

$z$ -polarized radiation,  $E_1$  excitons are allowed to emit  $xy$ -polarized radiation, while the rest are dark. Therefore, all lines in Figs. 3(a) and 3(b) correspond to  $A_1$  or  $E_1$  excitons. When the symmetry is lowered from  $C_{6v}$  to  $C_{3v}$ ,  $E_1$  and  $E_2$  become  $E$  which allows the emission of  $xy$ -polarized radiation,  $A_2$  and  $B_1$  become  $A_2$  which is dark, while  $A_1$  and  $B_2$  become  $A_1$  which allows the emission of  $z$ -polarized radiation. Therefore, the reduction in symmetry from  $C_{6v}$  to  $C_{3v}$  can transform dark excitons  $E_2$  and  $B_2$  into optically active ones.

Finally, we also discuss the degeneracy of the biexciton states. These are also represented by single-valued IRs of the symmetry group.<sup>40</sup> In the case when spin-orbit interaction is included, the biexciton state can have single or double degeneracy, as can be seen in Fig. 3(c). When it is not included, additional degeneracies exist due to spin part of the biexciton state, Fig. 3(d).

### C. Optimization of single GaN QDs for the single-photon sources applications

In this section, we present the calculations aimed to provide insight into the physical factors determining the performance of single-photon sources based on GaN/AlN quantum dots in general and, in particular, those reported in Ref. 16. The calculations of the single-particle electron and hole states and of the excitonic structure have been performed for a set of quantum dots satisfying the following conditions. The quantum-dot height was varied in the range of  $h=1.5-5$  nm with a step of 0.5 nm. The diameter to height ratio  $D/h$  was varied from 4 to 10 with a step of 1, and dots with the diameter larger than 30 nm were discarded. The truncated pyramid base angle of  $\alpha=30^\circ$  was assumed and the wetting-layer width of 0.5185 nm. The embedding box for electronic states with the diameter of  $D_e=50$  nm and height of  $H_e=10$  nm was used with the number of plane waves determined from  $(|n_1^{(e)}\rangle, |n_2^{(e)}\rangle, |n_3^{(e)}\rangle) = (6, 6, 12)$ . The corresponding box for evaluation of Fourier components of the strain and the potential arising from internal electric fields had the diameter  $D_s=150$  nm and the height  $H_s=180$  nm. The number of plane waves used to represent them was estimated by linear scaling as  $n_i^{(s)} = (D^{(s)}/D^{(e)})n_i^{(e)}$ ,  $i=\{1,2\}$ , and  $n_3^{(s)} = (H^{(s)}/H^{(e)})n_3^{(e)}$ , i.e.,  $(|n_1^{(s)}\rangle, |n_2^{(s)}\rangle, |n_3^{(s)}\rangle) = (18, 18, 216)$ . The necessity of employing such a large box is illustrated in Fig. 4. The dependences of energy levels on  $D_s$  and  $H_s$  [shown in Figs. 4(a) and 4(b)] enter saturation only when the chosen values of 150 and 180 nm, respectively, are reached. One can see from Figs. 4(c) and 4(d) that the internal-field-induced potentials dramatically differ if the values of  $D_e$  and  $H_e$  are chosen for  $D_s$  and  $H_s$ . The difference between the converged energies of eigenstates and the unconverged ones is mostly pronounced when the height of the embedding box is concerned [Fig. 4(b)]. The eigenvalues then differ by as much as 100 meV in the case of the electron ground state  $e0$  and 75 meV in the case of the hole ground state  $h0$ . We have also found that the values of all eigenenergies are more sensitive to the change in the size of the embedding box in the  $z$  direction than in the  $xy$  plane.

To ensure the convergence of Coulomb integral calculations, a box with the dimensions  $D_c=D_e=50$  nm, and

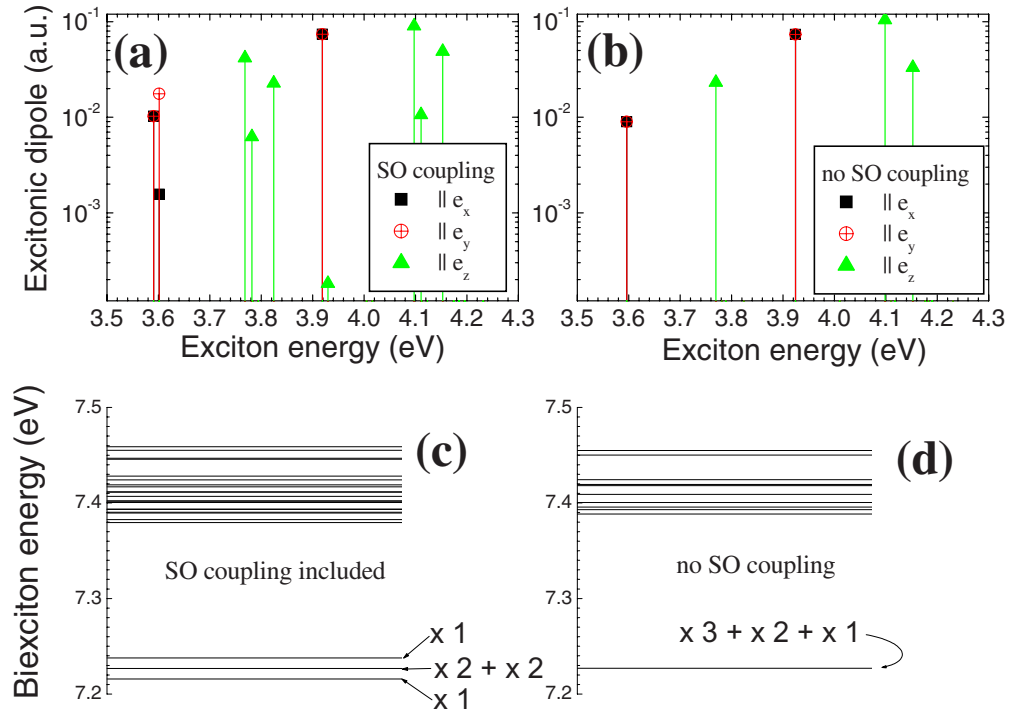


FIG. 3. (Color online) Influence of the spin-orbit interaction on the excitonic dipole elements [upper row: (a) and (b)] and biexcitonic structure [lower row: (c) and (d)] calculated by the CI method. In (a) and (c) the spin-orbit interaction is included while in (b) and (d) is ignored. Numbers in graphs for biexcitonic structure show the degree of degeneracy of a particular line. In some cases, these are closely spaced and can not be distinguished on the graphs.

slightly elongated along  $z$  direction to  $H_c = D_e/2$ , was used as described in Sec. III A. All CI calculations used the basis set consisting of  $N_e=8$  electron and  $N_h=14$  hole states (including the states of both spin). For all  $D/h$  ratios we get an expected result that the exciton energy  $E_X$  decreases as the quantum-dot height is increased, see Fig. 5(a). The same is the case when the energies of biexcitons  $E_{XX}$  are concerned, as can also be seen in Fig. 5(b).

The dependence of biexciton shift defined as

$$B_{XX} = E_{XX} - 2E_X \quad (8)$$

on exciton energy is presented in Fig. 6(a). It can be seen from this figure that for maximizing the biexciton shift smaller values of  $D/h$  ratio are required in agreement with the conclusion of Ref. 16. Within the fixed value of  $D/h$ , bigger dots tend to have larger values of the biexciton shift due to reduction in the attractive part of the Coulomb interaction, as explained in Sec. I.

On the other hand it is also important to have large values of optical dipole matrix elements on the exciton transition. These are presented in Fig. 6(b). Due to symmetry, the dipole matrix elements for the interaction with  $x$ - and  $y$ -polarized radiation are identical. One can conclude from this figure that larger  $D/h$  ratios are more desirable and that for a fixed  $D/h$  ratio, small quantum dots have much larger optical matrix elements. Unfortunately, the trends in dipole matrix elements are opposite to the trends in exciton shifts. Therefore, a compromise between these trends has to be made to find the optimal quantum-dot geometry.

To achieve this, we define the optimization function as

$$\Xi = (E_{XX} - 2E_X) \cdot \ln \left( \frac{p_X^{(x)}}{p_X^{(0)}} \right). \quad (9)$$

$p_X^{(x)}$  is the value of the  $x$  component of the dipole matrix element of the exciton transition,  $p_X^{(0)}$  is equal to  $10^{-4} p_X^{(x),\max}$ , and  $p_X^{(x),\max}$  is the maximal value of  $p_X^{(x)}$  for all quantum dots considered. While the choice of  $p_X^{(0)}$  is somewhat arbitrary, we find that the positions of maxima of the optimization function are weakly dependent on its value, when it is changed within reasonable limits. The dependence of the optimization function on exciton energy for different  $D/h$  ratios is presented in Fig. 7. For  $D/h=4$  and  $D/h=5$  the optimization function is nonmonotonous with a maximum at  $h=2.5$  and  $h=2.0$  nm, respectively. For larger  $D/h$  the largest value of optimization function is reached for the smallest dots among those investigated with the height of  $h=1.5$  nm. The most optimal dots emit in the range of 3.2–3.8 eV, as can be seen in Fig. 7. Experimental results on single-photon sources operating at 200 K reported in Ref. 16 show the emission energy of around 3.5 eV and are in very good agreement with our theoretical predictions presented here. This also suggests that their QD geometry is most likely very close to an optimal one. It was reported in Ref. 16 that the estimated dimensions of the dots based on atomic-force microscopy (AFM) measurements are: the height of 4 nm and the diameter of 25 nm. Our calculation for these dimensions of QDs yields an emission energy of 1.5 eV only, as well as very low values of the optimization function. However, AFM is a surface technique that measures the uncapped dots. Significant

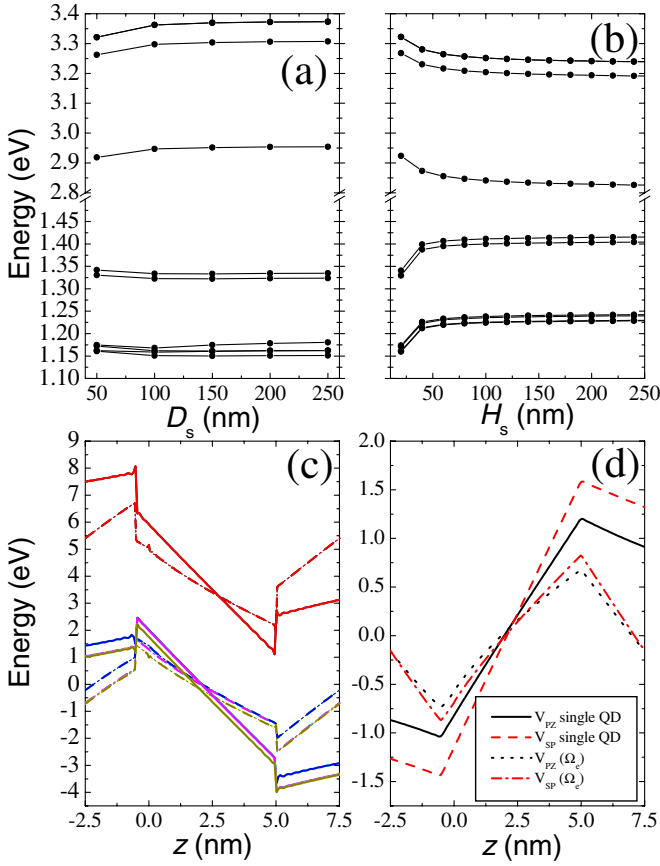


FIG. 4. (Color online) The dependence of electron and hole energies on (a) the diameter  $D_s$  of the box used for the calculation of strain; (b) the height  $H_s$  of the box used for the calculation of strain. (c) The effective electron and hole [from top of the valence band: crystal-field split-off hole (CH) band, light-hole (LH) band and heavy-hole (HH) band] potential when  $D_s=150$  nm and  $H_s=180$  nm (solid line) and  $D_s=D_e=50$  nm and  $H_s=H_e=10$  nm (dashed-dotted line). CH and LH almost overlap each other. (d) The contributions of spontaneous and piezoelectric polarization-induced potentials in these two cases. QD dimensions are  $D=25$  nm,  $h=5$  nm, and  $\alpha=30^\circ$ .

changes in the geometry of the dots after capping are possible and we believe that the dots measured in Ref. 16 actually have a much smaller height (i.e., reduced effective confinement region) than reported based on AFM measurements.

#### D. Effect of bound biexcitons in single GaN QDs

Another fundamental question related to the excitonic structure in GaN/AlN quantum dots, raised by the recent experiments<sup>15,25</sup> is the sign of the biexciton shift, i.e., whether the biexcitons are bound or unbound. For all calculations reported so far in this paper and in several earlier experiments<sup>12,16</sup> biexcitons are unbound. In recent single-dot spectroscopy experiments,<sup>15,25</sup> bound biexcitons have been measured as well for small quantum dots. While theoretical approaches based on Hartree approximation<sup>16,23</sup> are not capable of describing bound biexcitons due to lack of the electron correlation effects in the model,<sup>15,26</sup> the CI based approach should be, in principle, capable of doing that. In small

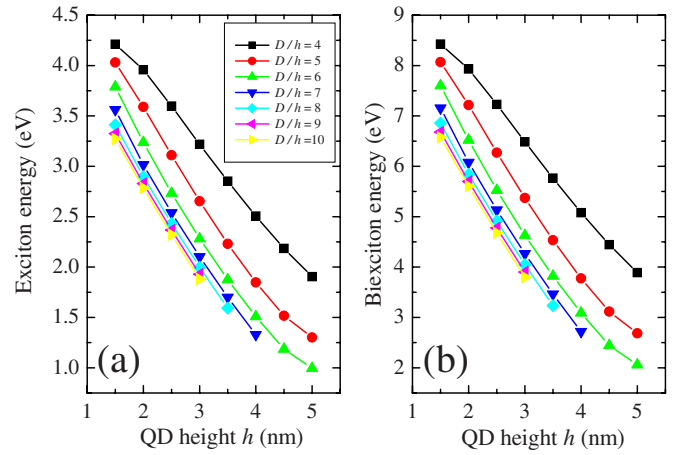


FIG. 5. (Color online) The dependence of ground (a) exciton and (b) biexciton energy on quantum-dot height for different values of diameter to height ratios  $D/h$ .

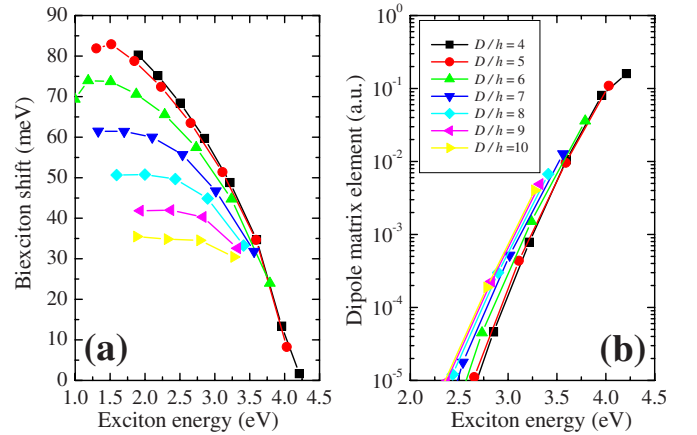


FIG. 6. (Color online) (a) The dependence of the biexciton shift,  $B_{XX}$  on exciton energy for different values of diameter to height ratios. (b) The dependence of the optical matrix elements,  $p_X^{(x)}$ , of the exciton transition on exciton energy for different values of diameter to height ratios  $D/h$ .

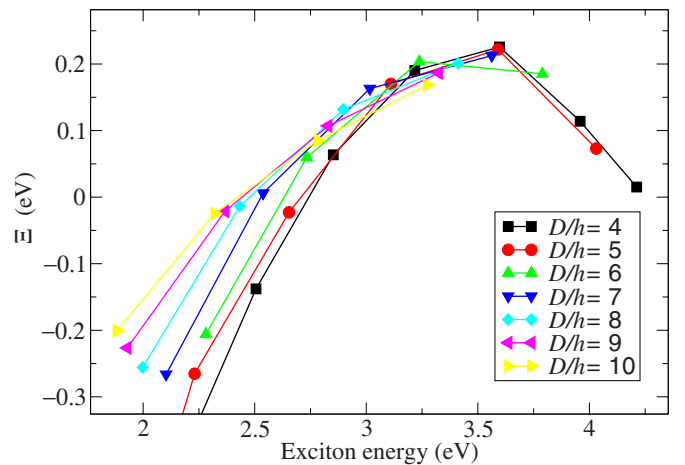


FIG. 7. (Color online) The dependence of the optimization function defined as  $\Xi(E_X)$  (see text for details) on exciton energy for different values of diameter to height ratios  $D/h$ .

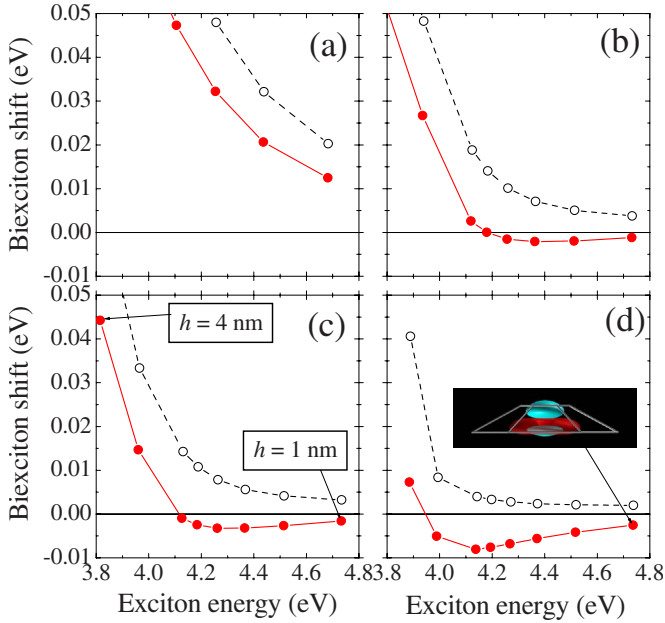


FIG. 8. (Color online) The dependence of biexciton shift on exciton energy for quantum dots with  $D/h=3$ ,  $h \in (1, 1.2, 1.4, 1.6, 1.8, 2, 3, 4)$  nm and spontaneous polarization multiplied by  $a$  and piezoelectric polarization multiplied by  $b$  in the cases: (a)  $a=1$  and  $b=1$ ; (b)  $a=1/3$  and  $b=0$ ; (c)  $a=0$ ,  $b=1/3$ ; (d)  $a=0$  and  $b=0$ . CI calculation with  $N_e=8$  electron and  $N_h=14$  hole states (solid lines) and  $N_e=2$  and  $N_h=2$  (dashed lines) corresponding to the Hartree approximation is presented. In (c) the height of the QD for the end points is specified and is the same for all four graphs. The inset in (d) depicts topmost (eighth) electron and lowest (14th) hole state used in CI calculations for the smallest QD in the series ( $D=3$  nm and  $h=1$  nm) that are still well localized to the QD region.

QDs, the exchange-correlation effect might be sufficient to compensate for the increase in the direct Coulomb energy of two excitons in a QD. In those QDs the exchange-correlation effect could be potentially pronounced since one might expect that piezoelectric and spontaneous polarization effects are reduced due to QD size effect and therefore not capable of simultaneously reducing the electron-hole attraction (and exchange-correlation) and increasing the pairwise Coulomb repulsion.

There are however, several issues that one should consider related to the calculations for small dots, such as whether the models for polarizations work for such small dots, whether the envelope function theory is reliable, and whether there are enough bound states for convergent CI calculation. Putting these issues aside for the moment, we have calculated the excitons and biexcitons for a series of *small* dots with  $D/h=3$  since by looking at Fig. 6 and performing an extrapolation one may expect that bound biexcitons might appear then. The QD height was changed in the range of  $h \in (1, 1.2, 1.4, 1.6, 1.8, 2, 3, 4)$  nm,  $D/h=3$ , and the shape was controlled by  $\tan(\alpha)=2h/(D-1)$  nm. The results that are presented in Fig. 8(a) show biexcitons are strongly unbound if coefficients of the spontaneous polarization  $P_{sp}$  are  $-0.034$  and  $-0.090$  C/m<sup>2</sup> for GaN and AlN, respectively, and piezoelectric constants that enter the for-

mula for strain-induced polarizations are  $d_{15}=0.326$  and  $0.418$  C/m<sup>2</sup>,  $d_{13}=-0.527$  and  $-0.536$  C/m<sup>2</sup>, and  $d_{33}=0.895$  and  $1.561$  C/m<sup>2</sup> for GaN and AlN, respectively.<sup>33</sup>

We have checked that all states ( $N_e=8, N_h=14$ ) used for CI calculations, even in the smallest QD considered, are bound states [see Fig. 8(d)]. In contrast to InAs/GaAs where there are not enough bound states to perform convergent CI calculations,<sup>26</sup> much larger band offsets and effective masses of GaN/AlN system allow for enough bound states even for small dots.

We also expect that the envelope function approximation is still reliable as the heights of the dots presented in Fig. 8 are all larger than four monolayers. To gain insight into what would be the effect on changes in polarizations on biexciton shifts, we have calculated the excitons and biexcitons with artificially reduced values of spontaneous and piezoelectric polarization. The cases where the polarizations have been completely turned off or reduced to one third were considered. As can be seen from Figs. 8(b)–8(d), bound biexcitons were obtained only with both polarizations turned off or with one of the polarizations reduced to a third and the other one turned off. In all other cases the biexcitons are still not bound. The results of the calculation in the Hartree approximation are also shown in Fig. 8, (dashed line) to verify that the bound biexcitons cannot be obtained then. Our theoretical predictions of the bound biexciton appearance in the vicinity of the excitonic energy of  $\sim 4$  eV are in very good agreement with recent experimental findings.<sup>15</sup> These results suggest that it might be possible that the values of polarizations are reduced in comparison to what is expected from the existing theoretical models applied to such small dots. A more elaborate theory of the group III-nitrides material parameters<sup>51–53</sup> and nanostructures based on them, in particular, would be probably required to safely resolve these issues. Such theory should be based on *ab initio* calculations of polarizations in nitride nanostructures and is an interesting topic for future studies.

#### IV. CONCLUSIONS

In conclusion, the excitonic structure of GaN/AlN quantum dots was investigated and optimal-dot dimensions for single-photon source applications were found. For diameter to height ratios in the range of 6–10 the dots should be as small as possible while for smaller ratios there exist an optimal quantum-dot height. Our predictions that the optimal dots emit in the range of 3.2–3.8 eV are in very good agreement with the experimental results on existing single GaN quantum-dot sources, underpinning the validity of the model described here and QD morphology extracted from it. The importance of including the effect of spin-orbit interaction was demonstrated and shown that the models with  $C_{3v}$  and  $C_{6v}$  symmetry yield exactly the same degeneracies of single-particle and (multi)exciton states. The lower symmetry of the  $C_{3v}$  group is only manifested via some optical transitions that become weakly allowed. We also show that the existence of bound biexcitons in small GaN/AlN quantum dots cannot be reliably described with current approaches and parameter sets, which led us to question the use of the models for internal electric fields in such small dots.

## APPENDIX

Further reduction in the computational cost is achieved by exploiting the symmetry of the system.<sup>34,54</sup> The use of symmetry leads to block diagonalization of the Hamiltonian matrix, expanded in the PW basis, to  $M$  smaller matrices of approximately equal size and therefore to a reduction in the computational cost and memory requirements by a factor of  $M^2$ . This is achieved by making a unitary transformation from the plane-wave basis  $|\mathbf{k}, b\rangle$  (denoting the basis state where the envelope function of band  $b$  is equal to  $e^{i\mathbf{k}\mathbf{r}}$  and the other envelope functions are zero) to the basis of the states characterized by a given value of the  $z$  component of the total quasiangular momentum  $m_f$ . In the case of  $M$ -fold symmetry, the elements of this basis are given as

$$|m_f, \mathbf{k}, b\rangle = \frac{1}{\sqrt{M}} \sum_{l=0}^{M-1} e^{il\phi[m_f - J_z(b)]} |R_{l\phi}\mathbf{k}, b\rangle \quad (\text{A1})$$

with  $\mathbf{k}$  vectors satisfying  $k_x^2 + k_y^2 > 0$  and  $0 \leq k_y < \tan(\phi)k_x$ , and

$$|m_f, \mathbf{k}, b\rangle = |\mathbf{k}, b\rangle \quad (\text{A2})$$

with  $\mathbf{k}$  vectors satisfying  $k_x = k_y = 0$  and the band  $b$  satisfying  $\{J_z(b) - m_f \equiv 0 \pmod{M}\}$ . In previous equations  $\phi = 2\pi/M$ ,  $J_z(b)$  is the  $z$  component of the total angular momentum of the Bloch function of band  $b$ ,  $R_{l\phi}\mathbf{k} = \mathbf{k}'$  is the vector obtained by rotation of the vector  $\mathbf{k}$  by an angle  $l\phi$  around the  $z$  axis

$$k'_x + ik'_y = e^{il\phi}(k_x + ik_y),$$

$$k'_z = k_z, \quad (\text{A3})$$

while angular momentum  $m_f$  takes the values from the interval  $[-(M-1)/2, (M-1)/2]$  with a step of one. Previous formulas can be derived following the same approach as in Refs. 34 and 54. The symmetry of the 8-band model applied to highly symmetric hexagonal dot shapes embedded in hexagonal prism considered in this work is given by  $M=6$ . Since the diagonalization cost of the Hamiltonian matrix is proportional to third power of its rank,  $N_r^3$ , the total cost of the diagonalization is then  $\propto M \times (N_r/M)^3$ , which is 36 times faster than if the symmetry were not exploited.

\*stanko.tomic@stfc.ac.uk

- <sup>1</sup>F. Bernardini, V. Fiorentini, and D. Vanderbilt, *Phys. Rev. B* **56**, R10024 (1997).
- <sup>2</sup>V. Fiorentini, F. Bernardini, F. DellaSala, A. DiCarlo, and P. Lugli, *Phys. Rev. B* **60**, 8849 (1999).
- <sup>3</sup>D. Bouwmeester, A. Ekert, and A. Zeilinger, *The Physics of Quantum Information* (Springer, Berlin, 2000).
- <sup>4</sup>P. Michler, A. Kiraz, C. Becher, W. V. Schoenfeld, P. M. Petroff, L. D. Zhang, E. Hu, and A. Imamoglu, *Science* **290**, 2282 (2000).
- <sup>5</sup>C. Santori, M. Pelton, G. S. Solomon, Y. Dale, and Y. Yamamoto, *Phys. Rev. Lett.* **86**, 1502 (2001).
- <sup>6</sup>N. Akopian, N. H. Lindner, E. Poem, Y. Berlatzky, J. Avron, D. Gershoni, B. D. Gerardot, and P. M. Petroff, *Phys. Rev. Lett.* **96**, 130501 (2006).
- <sup>7</sup>R. M. Stevenson, R. J. Young, P. Atkinson, K. Cooper, D. A. Ritchie, and A. J. Shields, *Nature (London)* **439**, 179 (2006).
- <sup>8</sup>S. DeRinaldis, I. D'Amico, E. Biolatti, R. Rinaldi, R. Cingolani, and F. Rossi, *Phys. Rev. B* **65**, 081309(R) (2002).
- <sup>9</sup>B. Daudin, F. Widmann, G. Feuillet, Y. Samson, M. Arlery, and J. L. Rouvière, *Phys. Rev. B* **56**, R7069 (1997).
- <sup>10</sup>F. Widmann, J. Simon, B. Daudin, G. Feuillet, J. L. Rouvière, N. T. Pelekanos, and G. Fishman, *Phys. Rev. B* **58**, R15989 (1998).
- <sup>11</sup>A. D. Andreev and E. P. O'Reilly, *Phys. Rev. B* **62**, 15851 (2000).
- <sup>12</sup>S. Kako, K. Hoshino, S. Iwamoto, S. Ishida, and Y. Arakawa, *Appl. Phys. Lett.* **85**, 64 (2004).
- <sup>13</sup>C. Santori, S. Gotzinger, Y. Yamamoto, S. Kako, K. Hoshino, and Y. Arakawa, *Appl. Phys. Lett.* **87**, 051916 (2005).
- <sup>14</sup>A. F. Jarjour, R. A. Taylor, R. A. Oliver, M. J. Kappers, C. J. Humphreys, and A. Tahraoui, *Appl. Phys. Lett.* **91**, 052101 (2007).
- <sup>15</sup>D. Simeonov, A. Dussaigne, R. Butté, and N. Grandjean, *Phys. Rev. B* **77**, 075306 (2008).

- <sup>16</sup>S. Kako, C. Santori, K. Hoshino, S. Gotzinger, Y. Yamamoto, and Y. Arakawa, *Nature Mater.* **5**, 887 (2006).
- <sup>17</sup>R. Bardoux, T. Guillet, B. Gil, P. Lefebvre, T. Bretagnon, T. Taliercio, S. Rousset, and F. Semond, *Phys. Rev. B* **77**, 235315 (2008).
- <sup>18</sup>M. Winkelnkemper, R. Seguin, S. Rodt, A. Hoffmann, and D. Bimberg, *J. Phys.: Condens. Matter* **20**, 454211 (2008).
- <sup>19</sup>S. Nakamura and G. Fasol, *The Blue Laser Diode* (Springer, Berlin, 1997).
- <sup>20</sup>Y. Arakawa, *IEEE J. Sel. Top. Quantum Electron.* **8**, 823 (2002).
- <sup>21</sup>L. Nevou, F. H. Julien, M. Tchernycheva, F. Guillot, E. Monroy, and E. Sarigiannidou, *Appl. Phys. Lett.* **92**, 161105 (2008).
- <sup>22</sup>A. D. Andreev and E. P. O'Reilly, *Appl. Phys. Lett.* **79**, 521 (2001).
- <sup>23</sup>D. Williams, A. Andreev, and E. O'Reilly, *Superlattices Microstruct.* **36**, 791 (2004).
- <sup>24</sup>A. F. Jarjour, R. A. Oliver, A. Tahraoui, M. J. Kappers, C. J. Humphreys, and R. A. Taylor, *Phys. Rev. Lett.* **99**, 197403 (2007).
- <sup>25</sup>J. Renard, R. Songmuang, C. Bougerol, B. Daudin, and B. Gayral, *Nano Lett.* **8**, 2092 (2008).
- <sup>26</sup>O. Stier, *Electronic and Optical Properties of Quantum Dots and Wires* (Wissenschaft & Technik Verlag, Berlin, 2000).
- <sup>27</sup>V. Ranjan, G. Allan, C. Priester, and C. Delerue, *Phys. Rev. B* **68**, 115305 (2003).
- <sup>28</sup>S. Schulz, S. Schumacher, and G. Czycholl, *Eur. Phys. J. B* **64**, 51 (2008).
- <sup>29</sup>S. Schulz, S. Schumacher, and G. Czycholl, *Phys. Rev. B* **73**, 245327 (2006).
- <sup>30</sup>N. Baer, S. Schulz, P. Gartner, S. Schumacher, G. Czycholl, and F. Jahnke, *Phys. Rev. B* **76**, 075310 (2007).
- <sup>31</sup>M. Sénès, K. L. Smith, T. M. Smeeton, S. E. Hooper, and J. Heffernan, *Phys. Rev. B* **75**, 045314 (2007).
- <sup>32</sup>S. L. Chuang and C. S. Chang, *Phys. Rev. B* **54**, 2491 (1996).

- <sup>33</sup>I. Vurgaftman and J. R. Meyer, *J. Appl. Phys.* **94**, 3675 (2003).
- <sup>34</sup>N. Vukmirović, Z. Ikonić, D. Indjin, and P. Harrison, *J. Phys.: Condens. Matter* **18**, 6249 (2006).
- <sup>35</sup>O. Madelung, *Semiconductors: Data Handbook* (Springer, Berlin, 2004).
- <sup>36</sup>P. Tronc, K. S. Zhuravlev, V. G. Mansurov, G. F. Karavaev, S. N. Grinyaev, I. Milosević, and M. Damnjanović, *Phys. Rev. B* **77**, 165328 (2008).
- <sup>37</sup>M. Winkelnkemper, A. Schliwa, and D. Bimberg, *Phys. Rev. B* **74**, 155322 (2006).
- <sup>38</sup>N. Vukmirović and S. Tomić, *J. Appl. Phys.* **103**, 103718 (2008).
- <sup>39</sup>V. A. Fonoberov and A. A. Balandin, *J. Appl. Phys.* **94**, 7178 (2003).
- <sup>40</sup>P. Tronc, V. Smirnov, and K. Zhuravlev, *Phys. Status Solidi B* **241**, 2938 (2004).
- <sup>41</sup>R. Beresford, *J. Appl. Phys.* **95**, 6216 (2004).
- <sup>42</sup>M. Rontani, C. Cavazzoni, D. Bellucci, and G. Goldoni, *J. Chem. Phys.* **124**, 124102 (2006).
- <sup>43</sup>P.-O. Löwdin, *Phys. Rev.* **97**, 1474 (1955).
- <sup>44</sup>W. Sheng, S.-J. Cheng, and P. Hawrylak, *Phys. Rev. B* **71**, 035316 (2005).
- <sup>45</sup>G. Makov and M. C. Payne, *Phys. Rev. B* **51**, 4014 (1995).
- <sup>46</sup>A. Franceschetti, H. Fu, L. W. Wang, and A. Zunger, *Phys. Rev. B* **60**, 1819 (1999).
- <sup>47</sup>S. Tomić, A. G. Sunderland, and I. J. Bush, *J. Mater. Chem.* **16**, 1963 (2006).
- <sup>48</sup>M. Leslie and M. J. Gillan, *J. Phys. C* **18**, 973 (1985).
- <sup>49</sup>J. P. Elliott and P. G. Dawber, *Symmetry in Physics* (Macmillan, London, 1979).
- <sup>50</sup>T. Saito and Y. Arakawa, *Physica E* **15**, 169 (2002).
- <sup>51</sup>S. Tomić, B. Montanari, and N. M. Harrison, *Physica E* **40**, 2125 (2008).
- <sup>52</sup>P. Rinke, M. Winkelnkemper, A. Qteish, D. Bimberg, J. Neugebauer, and M. Scheffler, *Phys. Rev. B* **77**, 075202 (2008).
- <sup>53</sup>G. Bester, X. Wu, D. Vanderbilt, and A. Zunger, *Phys. Rev. Lett.* **96**, 187602 (2006).
- <sup>54</sup>N. Vukmirović, D. Indjin, V. D. Jovanović, Z. Ikonić, and P. Harrison, *Phys. Rev. B* **72**, 075356 (2005).